# Detection and Localization of Debonding beneath Concrete Pavement Using Transmissibility Function Analysis

Difei Wu[a, *], Mengyuan Zeng[a], Hongduo Zhao[a], Yang Wang[b,c] and Yuchuan Du[a]

a. Key Laboratory of Road and Traffic Engineering of the Ministry of Education, Tongji University, Shanghai, P. R. China
b. School of Civil and Environmental Engineering, Georgia Institute of Technology, Atlanta, GA, USA
c. School of Electrical and Computer Engineering, Georgia Institute of Technology, Atlanta, GA, USA

## Abstract

This paper proposes a novel method to detect and localize debonding beneath the concrete pavement using transmissibility function (TF) analysis. The layout of the measurement node array, the signal processing approach, and the testing procedures are proposed. Two matrices of transmissibility damage indicator (TDI) are proposed to describe the distribution of debonding. This method is a response-only approach and can offer advantages in easy and low-cost implementation. The theoretical deduction, finite element analysis (FEA), and field tests are conducted to demonstrate and verify detection and localization performance. It is first observed that the arrangement of measurement nodes and the frequency range are crucial to TF analysis. TFs at higher frequencies range are more sensitive to the debonding but may result in higher errors. The density of the measurement node array and the noise's effect are investigated in the FEA. Using a denser node array and maintaining a lower noise level helps localize the debonding more precisely. Field tests are conducted on a precast concrete pavement plate using a specially designed accelerometer array. The test results demonstrate the feasibility of the TF-based method for debonding detection and localization.

**Keywords:** concrete pavement, debonding, transmissibility function, transmissibility damage indicator, detection and localization

## 1. Introduction

Concrete pavement is one of the largest infrastructures in many countries and is widely used in highways and airport runways. Timely and effective structural health monitoring (SHM) is required for pavement asset management and pavement maintenance. For concrete pavement, debonding is one of the most common distress that occurs under the concrete pavement plate. Interface debonding is associated with the support condition under the concrete pavement. Severe debonding can result in irreversible distresses, such as joint faults and cracking [1]. Therefore, it is of great importance to detect support-loss at the early stages. Additionally, debonding is more likely to occur at the corner of the concrete plate and then expands along the edge.

Unlike some typical distresses in concrete pavement such as cracking and pothole, debonding is invisible distress, which is more difficult to detect. Traditional methods use non-destructive testing devices such as falling weight deflectometers (FWD), ground penetration radar (GPR), and ultrasonic arrays to capture the information of support conditions under the concrete plate. Among these methods, the FWD is the most common-used device in many countries. The rationale behind the FWD-based method is that debonding increases the surface deflections under a constant impact load [2][3]. This method is a response-based way that identifies the debonding using a known excitation and several deflection measurements, but it still has some shortages, such as time-consuming and high operation costs.

Vibration testing is another response-based way that relies on the principle that debonding affects the pavement structure's frequency response function (FRF). The pavement plate can be modeled as a thin plate on an elastic foundation for concrete pavement structure. Therefore, debonding would change the support condition of the thin plate and further affect the FRF. Based on this idea, many studies were conducted to discover how debonding affects the FRF. Early researches mainly focus on the modal properties of the concrete pavement structure. Song derived an equation and showed the relation between the model frequencies and the foundation properties, indicating that poor support condition reduces the modal frequencies [4]. This result was also demonstrated in finite element analyses and field tests. With the application of some novel signal processing methods, Zhao et al developed a vibration monitoring system to identify debonding and evaluate the support condition under the concrete pavement [5]. Although the monitoring system can detect the debonding with relatively low-cost equipment, this system still requires a standard impact load and cannot provide precise location information of the debonding. To this end, this paper attempts to use an output-only approach to avoid applying a standard impact load in vibration tests. Among current output-only techniques, transmissibility functions (TFs), which can avoid measuring the input and assuming specific models for the input, have proven to be an attractive tool for structural damage identification [6–8] and operational modal analysis [9].

A TF was defined as the ratio of two FRFs related to the mass distribution, stiffness properties, and damping properties of the system [10]. Through comparing the differences of two TFs under intact and damaged conditions, the typical structural damages, including mass loss and stiffness loss, can be determined and localized. As one of the most common-used output-only approaches, the TF was firstly proposed in 1994 for structural faults detection [11]. In the following decades, many researchers conducted theoretical deductions, finite element analyses, and laboratory tests to study the TF-based methods for damage detection on different structures, including chain-like multi-degree-of-freedom systems [12], beams [13], multi-story buildings [14], frames [15], and even tunnel [16] and bridge [17]. More recently, emerging sensing technologies were introduced in laboratory experiments. Yi and Zhu [14,15] developed a mobile sensing system capable of maneuvering on the surface of ferromagnetic materials, and then applied this system to capture TFs for damage detection frame structure and a multi-story building structure.

For a linear system, the TF-based method is useful for structural damage identification and localization, but it strongly depends on the layout of measurement nodes and the frequency ranges. For concrete pavement structure, the debonding can be regarded as stiffness losses in a linear system, indicating that TF has the potential in debonding localization and detection. In this paper, theoretical deduction, FEA, and field tests were conducted to study the performance of TF in debonding detection and localization. The following sections present the principle of TF, the numerical simulations, and the validation results in experiments.

## 2. Principle of Transmissibility Function

### *2.1 Transmissibility function algorithm*

For a stable multi-degrees-of-freedom linear dynamic system, the equations of motion are formulated as:

$$\boldsymbol{M}\ddot{\boldsymbol{x}}(t) + \boldsymbol{C}\dot{\boldsymbol{x}}(t) + \boldsymbol{K}\boldsymbol{x}(t) = \boldsymbol{F}(t) \tag{1}$$

where the **M**, **C**, and **K** are the mass, damping and stiffness matrices, respectively; $\ddot{\boldsymbol{x}}(t)$, $\dot{\boldsymbol{x}}(t)$ and $\mathbf{x}(t)$ denote the displacement, velocity and acceleration vectors of the MDOF system, respectively; $\mathbf{F}(t)$ denotes the external excitation.

For a harmonic excitation, Eq. (1) can be represented in the frequency domain by the Laplace transform:

$$\mathbf{X}(\omega) = \mathbf{H}(s)\mathbf{F}(s) = (s^2\mathbf{M} + s\mathbf{C} + \mathbf{K})^{-1}\mathbf{F}(s) \tag{2}$$

where $\mathbf{H}(s) = (s^2\mathbf{M} + s\mathbf{C} + \mathbf{K})^{-1}$ is the displacement frequency response function (FRF) matrix. The FRF matrix represents the system response characteristics in the frequency domain, and it can be measured from experiments or finite element analysis.

Then the acceleration response in the frequency domain can be obtained from Eq. (2) as:

$$\mathbf{A}(s) = s^2\mathbf{H}(s)\mathbf{F}(s) \tag{3}$$

The transmissibility function is defined as the ratio between the two acceleration responses at the *i*-th and *j*-th DOFs ( $A_i(s)$ and $A_j(s)$ )：

$$T_{ij}(s) = \frac{A_i(s)}{A_j(s)} \tag{4}$$

Assume that only one external excitation $F_k(t)$ is applied on the *k*-th DOF of the system, as expressed in Eq. (5).

$$\mathbf{F}(s) = \{0, 0, 0, \ldots, f(s), \ldots 0\} \tag{5}$$

and then substituting $\mathbf{F}(s)$ in Eq. (3) into Eq. (4). $T_{ij}(s)$ can be calculated as：

$$T_{ij}(s) = \frac{H_{ik}(s)\mathbf{F}(s)}{H_{jk}(s)\mathbf{F}(s)} = \frac{H_{ik}(s)}{H_{jk}(s)} \tag{6}$$

where $H_{ik}(s)$ denotes the FRF between *i*-th and *k*-th DOF, and $H_{jk}(s)$ denotes the FRF between *j*-th and *k*-th DOF. As shown in Eq. (6), the transmissibility function is an output-only measurement, which only depends on the location of the force and the FRF matrix.

*2.2 TF-based damage indicator*

In damage detection and localization, the recommended method is to capture the tracking of the changes of the TFs at specific frequencies or over certain frequency bands. For this purpose, several damage indicators were introduced and used by many authors. Among them, the research group at the National Aeronautics and Space Administration (NASA) Center for Aerospace Research proposed a widely-used damage indicator based on the integral over a frequency band of the difference between TFs corresponding to the intact and damaged states [18]:

$$TDI_{ij} = \frac{\int_{\omega_1}^{\omega_2} \left| T_{ij}^U - T_{ij}^D \right| d\omega}{\int_{\omega_1}^{\omega_2} \left| T_{ij}^U \right| d\omega} \tag{7}$$

where $\omega_1$ and $\omega_2$ are the lower and upper bounds of the interested frequency range, superscript '*U*' represents the undamaged structure, and superscript '*D*' represents the damaged structure. Accordingly, $T_{ij}^U$ represents the transmissibility function of the undamaged structure and $T_{ij}^D$ represents the transmissibility function of the damaged structure. In some specific scenarios, the *TDI* is defined in the logarithmic scale to emphasize the effect of overall waveform differences and suppress occasional sharp peaks that may occur in practice [16].

$$TDI_{ij} = \frac{\int_{\omega_1}^{\omega_2} \left| \log\left| T_{ij}^U \right| - \log\left| T_{ij}^D \right| \right| d\omega}{\int_{\omega_1}^{\omega_2} \left| \log\left| T_{ij}^U \right| \right| d\omega} \tag{8}$$

*2.3 TF in concrete pavement*

A typical concrete pavement is a multi-layer structure that consists of the concrete plate, the base layer, and the soil foundation. To simplify this structure for transmissibility function analysis, we firstly model the pavement structure as a beam on a Winkler foundation, as shown in Figure 1. The beam is then discretized to form a chain-like n-DOF linear system, a common-used example in current studies.

In most studies, researchers care about the effect of stiffness and mass change on the transmissibility functions as the FRF strongly depends on the two parameters. For the concrete pavement structure, the debonding can be regarded as the stiffness change under the beam. In Figure 1, it is seen that the springs in the n-DOF system are classified into three classes: the ground spring ($k_g$) that depends on the support condition, the joint spring ($k_t$) that depends on the joint load transfer condition, and the inner spring ($k$) that depends on the stiffness of the pavement structure. Assumed that the debonding only affects the support condition, we can introduce the debonding by removing or reducing the stiffnesses of the ground springs under the corresponding DOFs.

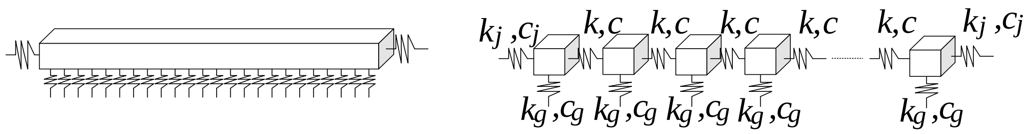


**Figure 1. *n*-DOF system of the pavement beam**

For the beam-like pavement structure, the matrices in Eq. (1) can be expressed as follows:

$$\boldsymbol{M} = Diag\{m, m, m \cdots m\} \tag{9}$$

$$\boldsymbol{K} = \begin{bmatrix} k_g + k + k_t & -k & 0 & \cdots & 0 \\ & 2k + k_g & -k & \cdots & \vdots \\ & & \ddots & \ddots & 0 \\ & \text{Symm.} & & 2k + k_g & -k \\ & & & & k_g + k + k_t \end{bmatrix} \tag{10}$$

$$\boldsymbol{C}=\begin{bmatrix} c_g+c+c_t & -c & 0 & \cdots & 0 \\ & 2c+c_g & -c & \cdots & \vdots \\ & & \ddots & \ddots & 0 \\ & \text{Symm.} & & 2c+c_g & -c \\ & & & & c_g+c+c_t \end{bmatrix} \tag{11}$$

The FRF matrix is then deduced as follow:

$$\mathbf{H}(s)=\mathbf{B}(s)^{-1} \tag{12}$$

where,

$$\boldsymbol{B}(s)=(s^2\boldsymbol{M}+s\boldsymbol{C}+\boldsymbol{K})$$

$$=\begin{bmatrix} ms^2+s(c_g+c_t+c)+k+k_g+k_t & -sc-k & 0 & \cdots & 0 \\ & ms^2+s(c_g+2c)+2k+k_g & -sc-k & \ddots & \vdots \\ & & \ddots & \ddots & 0 \\ & \text{Symm.} & & \ddots & -sc-k \\ & & & & ms^2+s(c_g+c_t+c)+k+k_g+k_t \end{bmatrix} \tag{13}$$

The entries in the inverse of a tridiagonal matrix can be expressed in a recursive form [19], where the complex argument '(s)' is neglected hereinafter to lighten the notation:

$$H_{ij}=\begin{cases} U_iU_{i+1}\cdots U_{j-1}H_{jj} & i<j \\ H_{ji} & i>j \\ [B_{ii}-X_i-Y_i]^{-1} & i=j \end{cases} \tag{14}$$

where the U, X, Y are intermediate variables that are recursively computed based on the entries in matrix B(s), lecture [14] also produced the recursive relationship between $U_i$ and $U_{i-1}$, as shown in Eq. (13):

$$U_i=\frac{-B_{i(i+1)}}{B_{ii}+B_{i(i-1)}U_{i-1}}(i=2,\dots,N-1) \tag{15}$$

Based on this recursive form, we can then deduce the transmissibility functions between two adjacent DOFs with an external excitation applied at the latter DOF, as expressed in Eq. (16)

$$T_{i(i+1)}=U_i, i=1,2,\dots,N-1 \tag{16}$$

Also, we can extend this equation and deduce the transmissibility function $T_{ij}$ while an external excitation applied on the *k*-th DOF, assumed *i*<*j*<*k*, the transmissibility function can be expressed as:

$$T_{ij} = \frac{H_{ik}}{H_{jk}} = \frac{U_i U_{i+1} \cdots U_{k-1} H_{kk}}{U_j U_{j+1} \cdots U_k H_{kk}} = \prod_{n=i}^{j-1} U_n \tag{17}$$

Substituting Eq. (11) into Eq. (15), $U_1$ is calculated as:

$$\begin{aligned} U_1 &= \frac{-B_{12}}{B_{11}} \\ &= \frac{sc + k}{ms^2 + s(c_g + c_t + c) + k + k_g + k_t} \end{aligned} \tag{18}$$

When the complex argument *s* is large enough, which indicates at a higher frequency range, $U_2$ can be expressed as:

$$\begin{aligned} U_2 &= \frac{-B_{23}}{B_{22} + B_{12} U_1} \\ &= \frac{sc + k}{ms^2 + s(c_g + 2c) + 2k + k_g - \dfrac{(sc + k)^2}{ms^2 + s(c_g + c_j + c) + k + k_g + k_t}} \\ &\approx \frac{sc + k}{ms^2 + s(c_g + 2c) + 2k + k_g} \end{aligned} \tag{19}$$

Similarly, we can obtain the approximate expression of $U_i$:

$$U_i = \begin{cases} \dfrac{sc + k}{ms^2 + s(c_g + c_j + c) + k + k_g + k_t} & i = 1, N \\ \dfrac{sc + k}{ms^2 + s(c_g + 2c) + 2k + k_g} & i = 2, \dots, N-1 \end{cases} \tag{20}$$

Assume that a debonding occurs at the *h*-th DOF, which indicates that the $c_g$ and $k_g$ become zero at the *i*-th DOF, the corresponding $U_i$ becomes:

$$U_h^D = \begin{cases} \dfrac{sc+k}{ms^2+s(c_j+c)+k+k_t} & h=1,N \\ \dfrac{sc+k}{ms^2+2sc+2k} & h=2,\dots,N-1 \end{cases} \tag{21}$$

We can then obtain the TF at the two adjacent DOFs ($h$-th DOF and ($h$+1)-th DOF) and calculate the difference between the TFs that are before and after introducing the debonding, as shown in Eq. (22).

$$\begin{aligned} \varepsilon &= T_{h(h+1)}^D - T_{h(i+1)} \\ &= U_i^D - U_i \\ &= \begin{cases} \dfrac{sc+k}{ms^2+s(c_j+c)+k+k_t} - \dfrac{sc+k}{ms^2+s(c_g+c_j+c)+k+k_g+k_t} & i=1,N \\ \dfrac{sc+k}{ms^2+2sc+2k} - \dfrac{sc+k}{ms^2+s(c_g+2c)+2k+k_g} & i=2,\dots,N-1 \end{cases} \end{aligned} \tag{22}$$

Also, assume that the complex argument $s$ is large enough, Eq.(22) can be simplified as:

$$\varepsilon = \frac{(sc+k)(sc_g+k_g)}{m^2s^4} \tag{23}$$

We then assume that the debonding occurs at the $h$-th DOF and consider the following two debonding scenarios (Figure 2):


(a) $i \le h \le j$ (b) $h < i < j$ or $i < j < h$

**Figure 2. Two debonding scenarios**

(a) $i \le h \le j$

According to Eq. (20) and Eq.(17), the transmissibility function $T_{ij}$ would be affected, as expressed in Eq. (24).

$$T_{ij}^D = \prod_{x=i}^{h-1} U_x \cdot U_h^D \cdot \prod_{x=h+1}^{j-1} U_x \tag{24}$$

According to Eq. (23), the difference between $T_{ij}$ and $T_{ij}^D$ can be expressed as:

$$T_{ij}^D - T_{ij} = \prod_{x=i}^{h-1} U_x \cdot \prod_{x=h+1}^{j-1} U_x \cdot \frac{(sc+k)(sc_g+k_g)}{m^2 s^4} \tag{25}$$

(b) $h < i < j$ or $i < j < h$

According to Eq.(17), $T_{ij}$ is only determined by the DOFs between the *i*-th DOF and the *j*-th DOF, debonding at the *h*-th DOF has little effect on $T_{ij}$. Therefore, we can have the expression of $T_{ij}^D$:

$$T_{ij}^D = T_{ij} = \prod_{x=i}^{j-1} U_x \tag{26}$$

From Eq. (25) and (26) we can easily infer that a debonding only affects the TFs measured across the debonding region but has little effects on the TFs at other positions. Moreover, as shown in Eq. (25), the $U_x$, $(x = i, i+1, \dots h-1, h+1, \dots j-1)$ in Eq. (25) becomes smaller when the complex argument *s* becomes larger, resulting a smaller value of the transmissibility function difference. Since the magnitude of the complex argument *s* determines the frequency, it is crucial to select an appropriate frequency range during TF analysis, guaranteeing that the difference between $T_{ij}^D$ and $T_{ij}$ is easier to identify.

*2.4 TF measurement in a concrete pavement plate*

For practical TF measurement, researchers proposed several methods to localize the damages based on TF indicators. As discussed in Simon's review paper [10], the best solution to localize damages is to apply the excitation force next to the damage. Wang and his colleagues demonstrated the method's effectiveness in a 4-story building model and a steel frame structure[14,15]. However, this method requires plenty of measurements, which is inappropriate for TF measurement on concrete pavements. As Eq. (17) indicates that the TF $T_{ij}$ does not depend on the loading position, thus we can fix the loading position and arrange a denser sensor array to capture the TFs in the concrete pavement structure. As the concrete pavement is a two-dimensional plate-like structure, we proposed the measurement procedures as follows:

Step 1: arrange the accelerometer array on the pavement plate;

Step 2: apply an impact load on the center of the plate;

Step 3: collect the acceleration data and calculate the TFs.

It should be noted that the pairs in TF calculation are considered in two directions, as illustrated in Figure 3. The impact load is applied on the center of the concrete slab, whose dimension is $w \times h$. Assume that the vibration is transmitted from the center to the edges and measured by a $n \times n$ measurement nodes. For each measurement node ($i$, $j$), the node pairs are defined based on their positions, as shown in Eq. (27-28)

$$\text{Pair1}=\begin{cases}(i,j)-(i,j+1) & i<\dfrac{n}{2}\\ (i,j)-(i,j-1) & i>\dfrac{n}{2}\\ 0i=\dfrac{n+1}{2} & \end{cases} \tag{27}$$

$$\text{Pair2}=\begin{cases}(i,j)-(i+1,j) & j<\dfrac{n}{2}\\ (i,j)-(i-1,j) & j>\dfrac{n}{2}\\ 0 & j=\dfrac{n+1}{2}\end{cases} \tag{28}$$

It is noted that the ‘0’ in Eq. (27) and Eq. (28) denotes that the TF of this pair is zero, in other words, only one direction is considered for those pairs. Once the accelerations are collected at the pairs, two $n \times n$ TF matrices, $TDI_1$ and $TDI_2$, are generated for debonding identification, which corresponds to pair 1 and pair 2 in Eq. (27) and Eq. (28). Using this measurement method, we only require a one-time measurement to detect the debonding condition under the concrete pavement, which is more time-saving traditional deflection-based method (nine measurements required for each pavement plate).

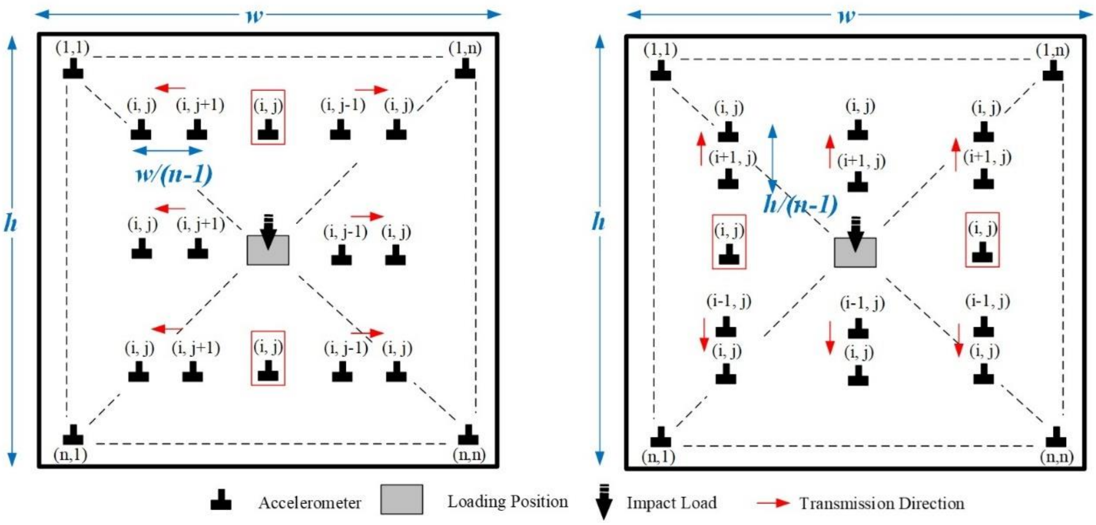


**Figure 3. Node pair determination in concrete pavement plate**

## 3. Numerical Simulation

Numerical simulations were conducted to study the feasibility and sensitivity of the TF-based method. To precisely model the concrete pavement, we established a nine-plate concrete pavement model in ABAQUS. Acceleration responses were obtained before and after introducing different types of debonding. This section describes the finite element analysis (FEA), the introductions of debonding and impulse excitations, and the TF calculations on the extracted accelerations.

*3.1 Finite Element Model*

A 3-D finite element model of a typical concrete pavement structure was developed in ABAQUS software to calculate the impact-induced accelerations (Figure 4). The central plate was used for acceleration extraction, while the adjacent eight plates were built to form the four joints. The pavement model also had a base layer and an elastic soil foundation. The Winker foundation model was used in FEA to simulate the soil foundation, which was modeled using the "Elastic Foundation Interaction" module in ABAQUS. As recommended in Chun's study [20], the interaction between the concrete plate and the base layer was determined using vertical spring elements (support springs) in ABAQUS. An eight-node linear brick element with reduced integration (C3D8R) was adopted for meshing the concrete pavement and base layer. Vertical spring elements were also used to simulate the interaction of joints. The geometric parameters and material properties are listed in Table 1.

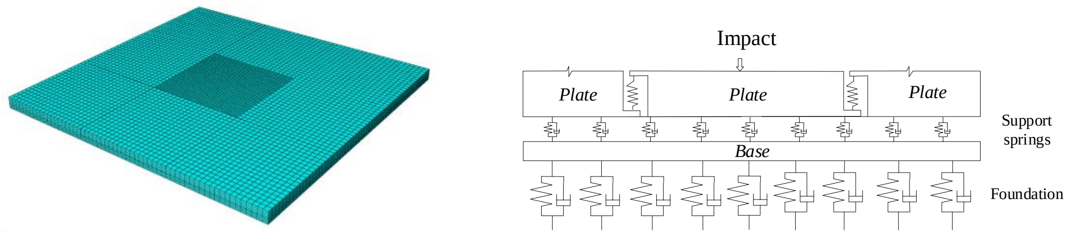


**Figure 4. Finite element model of concrete pavement**

**Table 1. Finite element analysis inputs**

| Layers | Parameters | Values |
|---|---|---|
| Plate | Dimensions /m × m × m | 4.0 × 4.0 × 0.24 |
| | Young's modulus /MPa | 36000 |
| | Poison's ratio | 0.15 |
| | Density / kg/m$^3$ | 2300 |
| | Rayleigh's damping coefficient | α=13.09, β=0.00019 |
| Base | Dimensions /m × m × m | 12 × 12 × 0.20 |
| | Young's modulus /MPa | 3000 |

| | | |
|---|---|---|
| | Poison’s ratio | 0.15 |
| | Density / $kg/m^3$ | 2300 |
| Foundation | Modulus of Winkler Foundation/（$MN/m^3$） | 80 |

*3.2 Debonding introduction*

Once a debonding occurs under the pavement plate, the vertical displacements and forces can hardly be transferred from the plate to the base layer. Therefore, debonding was simulated by removing the support spring elements at debonding regions.

*3.3 Excitation and acceleration acquisition*

In traditional pavement testing and evaluation, the falling weight deflectometer (FWD) is a common-used device that can easily apply an impact load using a drop weight. Therefore, we introduced the FWD load to stimulate vibrations in the FEM model. The loading position was set at the center in a shape of 30 cm × 30 cm square. The maximum load was set to be 50 kN.

When extracting the acceleration information, measurement points should be allocated uniformly on the plate. The layout of measurement nodes is crucial for practical measurement. Using a large number of measurement nodes can better capture the vibration information but cause a higher cost of testing. In contrast, using fewer measurement points can reduce the cost but may not guarantee identification accuracy. In the FEM model, four layouts with different densities of nodes were considered: 3 × 3, 5 × 5, 7 × 7, and 9 × 9. For an $n \times n$-size measurement nodes matrix, point (1, 1), point (1, $n$), point ($n$, 1) and point ($n$, $n$) were allocated at the four corners of the plate, and point (($n$+1)/2, ($n$+1)/2) was allocated at the center. Once the impulse excitation is applied, vertical acceleration data at the points are collected. The sampling frequency was set to 1000 Hz, the duration for each acceleration measurement was 0.5 seconds.

### *3.4 Scenarios*

The debonding under the concrete pavement is extremely complex. The debonding usually occurs at the corner and then expands along the edge. In some exceptional cases, the debonding occurs under the concrete slab's center due to differential settlements or inappropriate construction. Therefore, we considered four types of debonding in the FEA: debonding under the corner region (type 1), debonding under the edge region (type 2), debonding under the center region (type 3), and multi-region debonding (type 4). Type 1 and type 2 are the most common debonding in cast-in-situ concrete pavement. Type 3 debonding rarely occurs in the cast-in-situ pavement but may occur in some precast concrete pavement. Table 2 lists 11 typical scenarios debonding, including the dimensions and the corresponding schemes. It is noted that the planar shape of type 1 (debonding under the corner region) was assumed to be an isosceles right triangle, and the planar shape of type 2 (debonding under the edge region) was assumed to be a rectangle.

**Table 2. Debonding scenarios**

| No. | Scenarios | Scheme | No. | Scenarios | Scheme |
|---|---|---|---|---|---|
| 1 | No debonding | 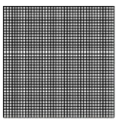 | 7 | Type 2,<br>300 cm × 60 cm | 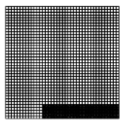 |
| 2 | Type 1,<br>40 cm-side length | 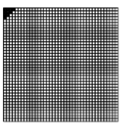 | 8 | Type 2,<br>400 cm × 60 cm | 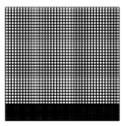 |
| 3 | Type 1,<br>60 cm-side length | 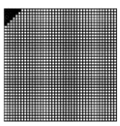 | 9 | Type 3,<br>40 cm × 40 cm | 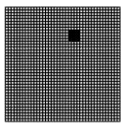 |

| No. | Scenarios | Scheme | No. | Scenarios | Scheme |
|---|---|---|---|---|---|
| 4 | Type 1,<br>80 cm-side length | 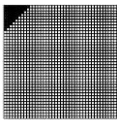 | 10 | Type 3,<br>60 cm × 60 cm | 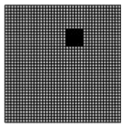 |
| 5 | Type 1,<br>120 cm-side length | 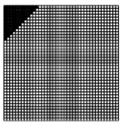 | 11 | Type 4,<br>(Scenario 3&5) | 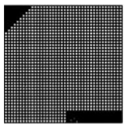 |
| 6 | Type 2,<br>200 cm × 40 cm | 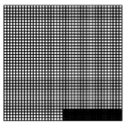 | 12 | Type 4,<br>(Scenario 4&7) | 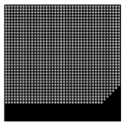 |

*3.5 TF calculation results*

This section presents the TF calculation results of each scenario. The 7 × 7 measurement nodes were firstly adopted to illustrate the effect of debonding under different regions. The node layout's and noise level's effects were then discussed based on Scenario 4 and 7.

(1) Debonding under the corner

Figure 5 shows the transmissibility functions between the location pairs of (1,1)-(1,2), (1,1)-(2,1), (1,7)-(1,6), and (1,7)-(2,7), the five curves in each sub-figure denotes the TFs of scenarios 1~5. The 'S *n*' (*n*=1,2,⋯⋯11) denotes the scenario *n* in Table 2. It is first observed that the variations of TFs are strongly related to the positions of debonding. The TFs vary significantly at the debonding regions while the TFs do not show noticeable differences in the other regions. It is also observed that the areas of debonding result in significant differences of TFs, and the differences mainly occur in the frequency range of 100~400 Hz, especially at around 180 Hz and 280 Hz. Since the selection of frequency range is crucial to damge identification, we considered the five frequency ranges for comparative analysis: 80~400 Hz, 100~400 Hz, 120~400 Hz, 140~400 Hz, and 160~400 Hz. The TDI values of the pair (1.1)-(1.2) were then calculated, as shown in Figure 6. It is observed that the frequency range of 160~400 Hz yields the maximum TDI value, indicating that the difference between TFs in damaged and undamaged is most significant in this frequency range. Therefore, we adopted this frequency range for further analysis.

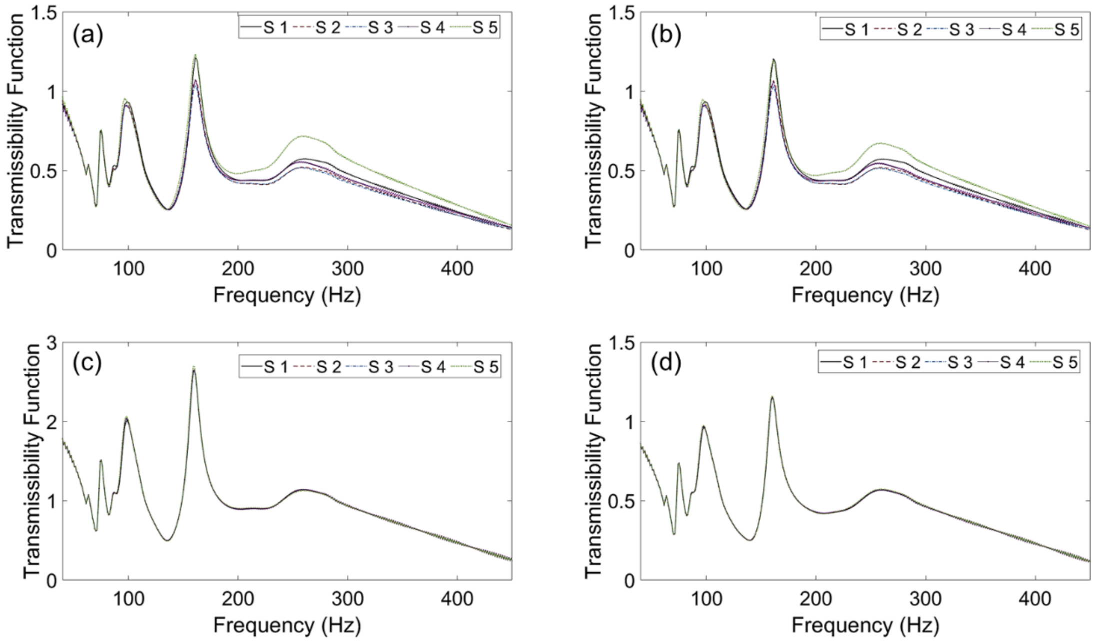


**Figure 5. TFs of: (a) pair (1,1)-(1,2); (b) pair (1,1)-(2,1); (c) pair (1,7)-(1,6); (d) pair (1,7)-(2,7)**

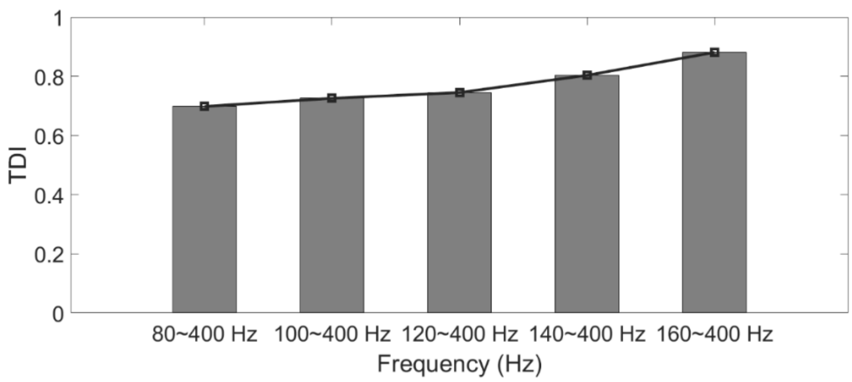


**Figure 6. TDI values in different frequency ranges (Scenario 3，pair (1.1)-(1.2))**

Figure 7 illustrated the two TDI matrices of scenarios 1~5. It is observed that the TDIs at corresponding points are much larger than the others. Furthermore, the range of debonding can be represented by the values and the distribution of the TDIs. For a slight debonding (≤0.16 m$^2$), the maximum TDI occurs at the point (1, 1) while the TDIs at other points is much smaller. For a severe debonding, the large TDIs occur in the corner region instead of one single point, the TDIs at point (1, 1), (1, 2), and (2, 1) are much higher than the TDIs at other points. Overall, the two TDI matrices demonstrate that this method is reliable for detecting and localizing the corner debonding.

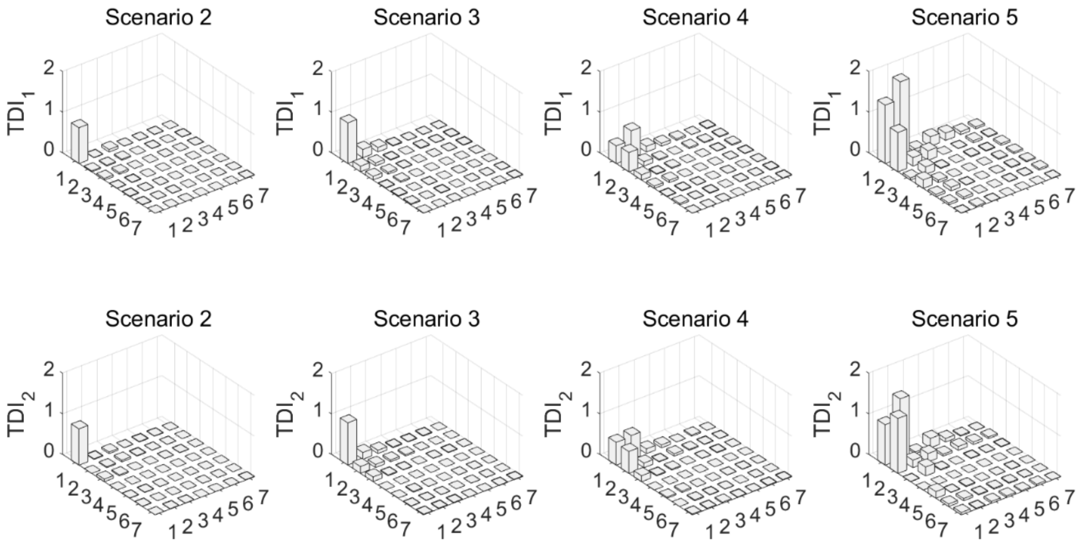


**Figure 7. TDI matrices of Scenarios 2~5 (debonding under the corner)**

(2) Debonding under the edge

Following the calculation procedure described above, the TDI matrices of scenarios 6~8 are calculated and shown in Figure 8. Note that the direction of $TDI_1$ is parallel to the debonding edge, while the direction of $TDI_2$ is perpendicular to the edge. Unlike the TDI matrices of the type 1-debonding, there are apparent differences between $TDI_1$ and $TDI_2$ in Figure 6. The TDI distributions in $TDI_2$ matrices match the distribution of debonding well, however, the distribution can hardly be observed in $TDI_1$ matrices. Using the perpendicular-TDI matrix is more appropriate to identify the debonding under the edges.

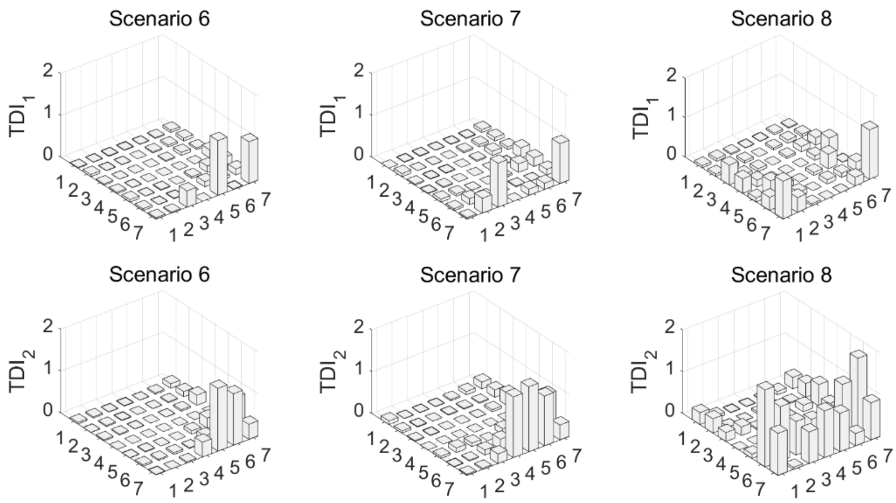


**Figure 8. TDI matrices of Scenarios 6~8 (debonding under the edge)**

(3) Debonding under the center region

The TDI matrices of scenarios 9~10 are illustrated in Figure 9. It is observed that the TDIs in the two matrices are very small (less than 0.05) compared with the TDIs in other scenarios. It is also seen that the maximum TDI occurs at the edge instead of the center, indicating that the debonding under the center region can hardly be identified from the two matrices.

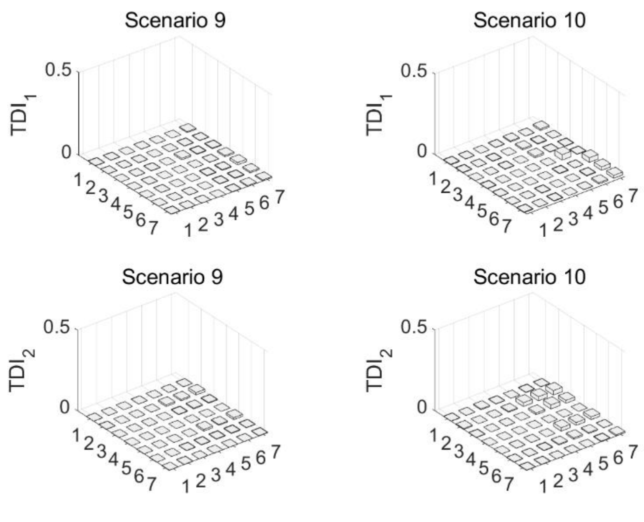


**Figure 9. TDI matrices of Scenarios 9~10 (debonding under the center)**

(4) Multi-region debonding

For multi-region debonding, we mainly consider the debonding occurring in both corner and edge regions. Figure 10 shows the TDI matrices of scenarios 11~12. Similar to the results in Figure 7 and Figure 8, the debonding under corners significantly increase the TDI values at corners, while the debonding under edges can only affect the TDI values in one direction. Therefore, we can easily infer that the multi-region debonding can also be detected through TF calculation.

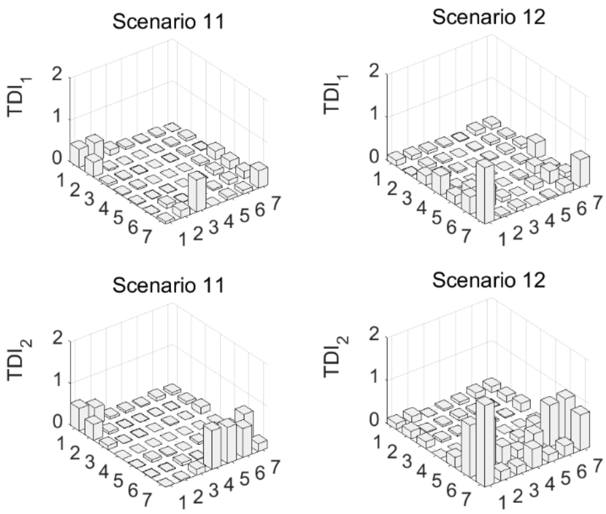


**Figure 10. TDI matrices of Scenarios 11~12 (multi-region debonding)**

(5) Effects of the layout of the measurement node array

The layout and the density of the measurement node array also affect the detection and localization performance. Figure 11 illustrates the TFs using different node arrays (Scenario 4). It is first observed that the magnitude of TF becomes smaller when the node array becomes denser. As expected, the apparent difference of TF is observed from all the four subfigures, indicating that the corner debonding can be well detected no matter what node array is used. Then, the TDI matrices of Scenario 4 and 7 were calculated, as shown in Figure 12 and Figure 13. As shown in the two figures, the denser node array provides more precise detection results. For instance, we can only identify the existence of a debonding at the corner from the TDI matrix of 3 × 3 node array, but the TDI values in the 9 × 9 matrix can estimate the range of the debonding at the corner. Additionally, the maximum TDI value may not occurs at the corners or edges when using a dense measurement node array. Figure 12 shows that the maximum TDI in 9 × 9 node array occurs at the debonding boundary position instead of the corner position. This pattern is also observed in Figure 13. Therefore, we can infer that the maximum value in a dense node array is able to identify the boundary of local debonding.

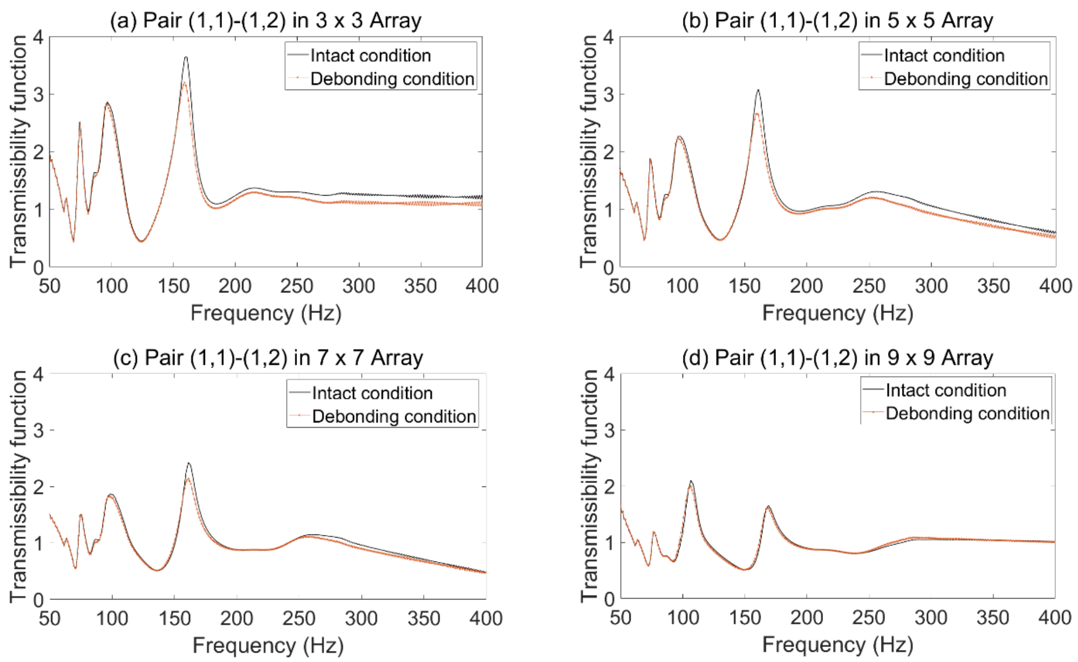


**Figure 11. TFs of different node array (Scenario 4)**

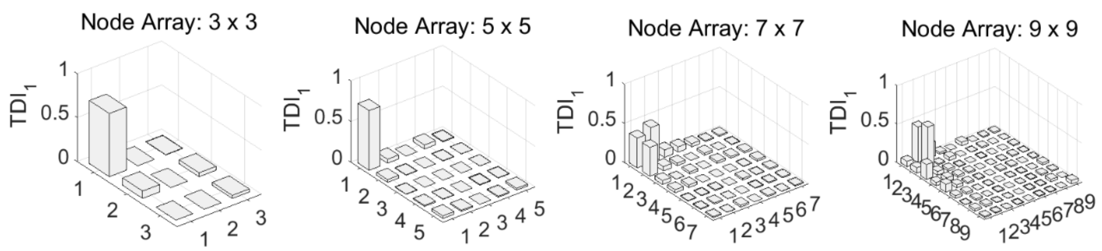


**Figure 12. TDI$_1$ matrices in different densities of node array (Scenario 4)**

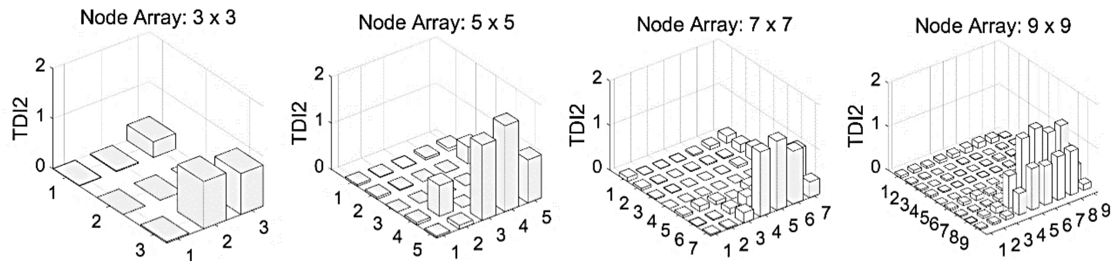


**Figure 13. $TDI_1$ matrices in different densities of node array (Scenario 7)**

(6) Effects of the noise level

In practical measurements, original signals rarely come clean. The noise level may have a significant effect on the TF analysis results. In this section, we compared the TF results in three noise levels: 0.01%, 0.1%, 1% and 3%, corresponding to the SNR of 40 dB, 30 dB, 20 dB and 15 dB. In the TF calculation, we take Scenario 4 as an example and generate the acceleration data by adding different white noises. Figure 14 illustrates the TDI matrices under such different noise levels. It shows a significant effect of the noise level on the detection results. When the noise level maintains a low level (SNR>20 dB), the debonding can still be detected and localized through the TDI matrix. A higher noise level (SNR=15dB) would increase the TDI values at intact regions. Once those TDI values exceed the maximum TDI in the matrix, it would cause detection errors. Therefore, it is recommended to apply the TF-based method at a low noise level and ensure that the SNR is no less than 30 dB.

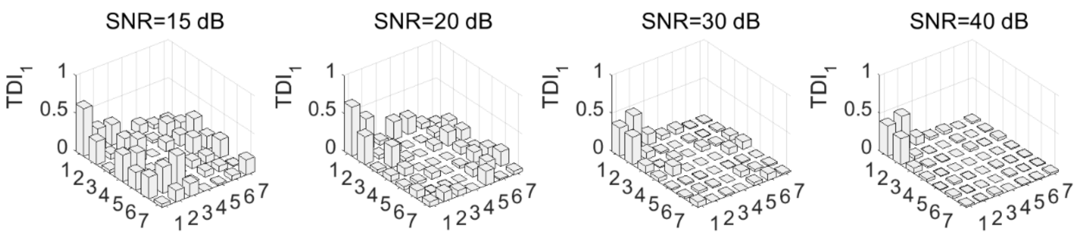


**Figure 14. $TDI_1$ matrices in different noise levels (Scenario 5)**

## 4. Experiments and Discussion

*4.1 Testbed structure*

A precast concrete pavement plate was constructed for field tests. As shown in Figure 15, the test plate's dimension is 2.5 m × 2.5 m × 0.25 m. Note that there was a thin grouting layer between the pavement plate and the base layer. During the grouting procedure, the boundary of the grouting layer can be formed using seal tapes. Therefore, we can form different types of debonding by adjusting the grouting boundary of the pavement plate. In this test, the type 4-debonding (multi-region debonding) was introduced, as shown in Figure 15(b).

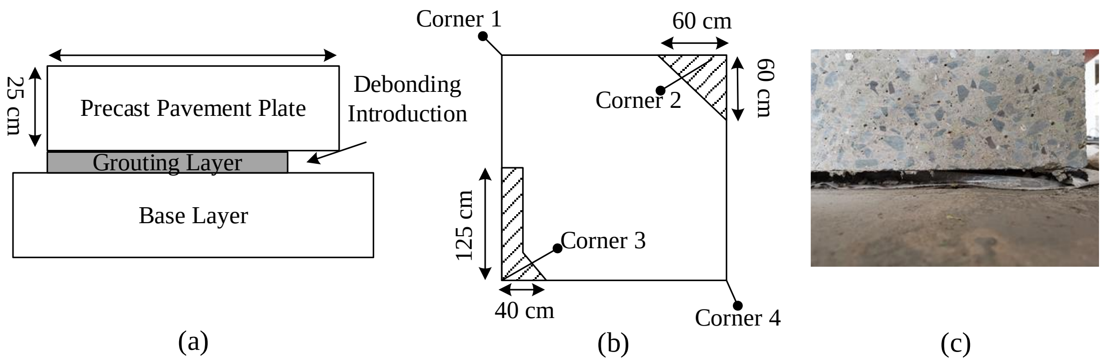


**Figure 15. (a) Testbed structure; (b) Debonding region; (c) Debonding at corner**

A series of accelerometers was introduced to capture the accelerations induced by an impulse load. The impulse load is applied using a portable falling weight deflectormeter (PFWD), which is a common-used device for pavement testing and can generate the impulse load using a falling weight. Table 2 shows the parameters of the PFWD device (Figure 16).

To form the accelerometer array, we designed a unique case equipped with a MEMS accelerometer and a heavy steel beam. The design of the beam-mounted accelerometer was referred to the Falling weight deflectometers, a widely-used device in pavement detection and evaluation. As shown in Figure 13(a)(c), the MEMS accelerometer is fixed on a flat plate. The flat plate has a long contact on the surface of the pavement to sense the surface vibration. The heavy beam was used to fix the accelerometers on the specific positions. When an impulse load vibrated pavement surface, the vibration of pavement surface would force the steel contact to vibrate. The steel contact vibration would then induce the plate vibration, which can be well measured by the mounted accelerometer. Note that the accelerometer was not connected directly to the heavy beam but connected through the four vertical springs. Since the spring stiffnesses were very small, the vibration of the beam can hardly affect the accelerometers. During the tests, the unique cases were firstly installed on two or three steel beams (Figure 17(d)), then, the spaces between the unique cases were adjusted to form a uniform accelerometer array. Once the impact load was applied on the center of the pavement plate, the vibration on the pavement surface would force the contacts in the unique cases to vibrate. The vibration signals were then sensed and collected through the MEMS accelerometers inside. Once one measurement was finished, the beam and the unique cases were moved for the next measurement.

**Table 3. Parameters of the PFWD**

| Parameter | Value |
|---|---|
| Height of drop weight /m | 0.7 |
| Weight /kg | 10 |
| Maximum impact force/kN | 10 |
| Loading radius/mm | 300 |
| Impact duration/ms | 17±1.5 |

**Figure 16. PFWD device**

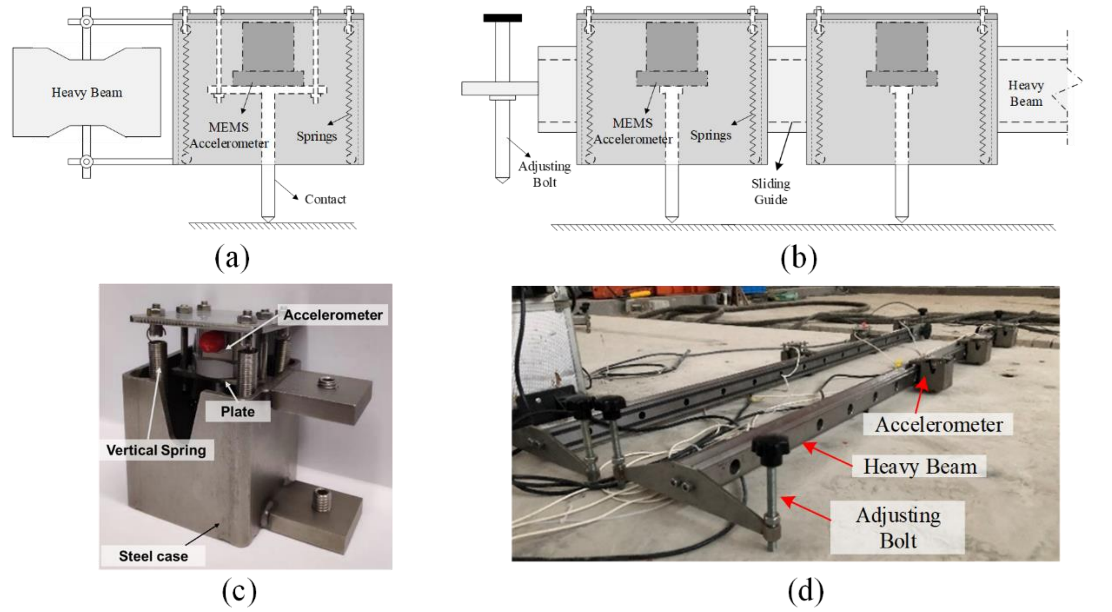


**Figure 17. Design and installation of accelerometers**

*4.2 Testing procedures*

As recommended in Section 3, a denser measurement node array provides more accurate detection performance. Therefore, we adopted a 7 × 7 node array in the experiment. In practical tests, it is difficult to arrange all the accelerometers and capture all acceleration time series simultaneously. We used a small accelerometer array (3 × 3) to solve this problem and move this array to capture the acceleration data at each pair of measurement node arrays, as shown in Figure 18. Nine measurements are required for the 7 × 7 array to cover all the node pairs. Moreover, to reduce the effect of experimental uncertainties, each measurement is repletely conducted three times. By adjusting the height of the drop weight in the FWD, the impact loads were applied at different levels, ranging from 1~10 kN. The sampling frequency for the acceleration measurement was set to be 5000 Hz. Once all measurements were finished, each pair's transmissibility functions were calculated and then used to calculate the TDI matrices for debonding detection and localization.

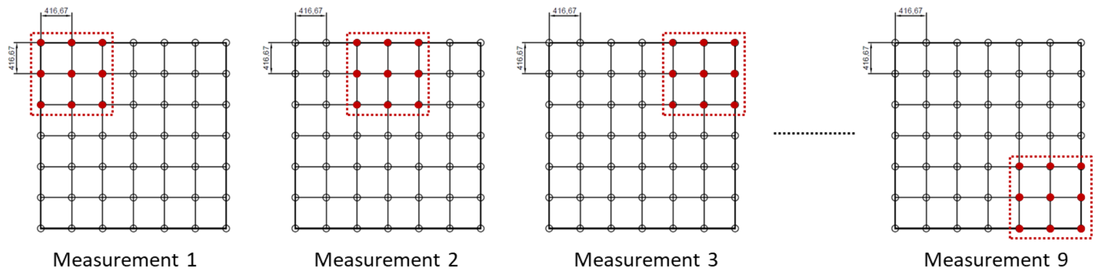


**Figure 18. Testing procedure**

*4.3 TF calculation*

Following the testing procedure described above, the acceleration data were captured before and after introducing the debonding. Before the TF calculation, a short-time energy (STE) method was first applied to capture the vibration signals in a long time series automatically. As shown in Figure 19, through sliding a 40 ms-width rectangular time window to cover the original time series, the time period of vibration can be located and extracted by searching the peaks in the short-time energy curve.

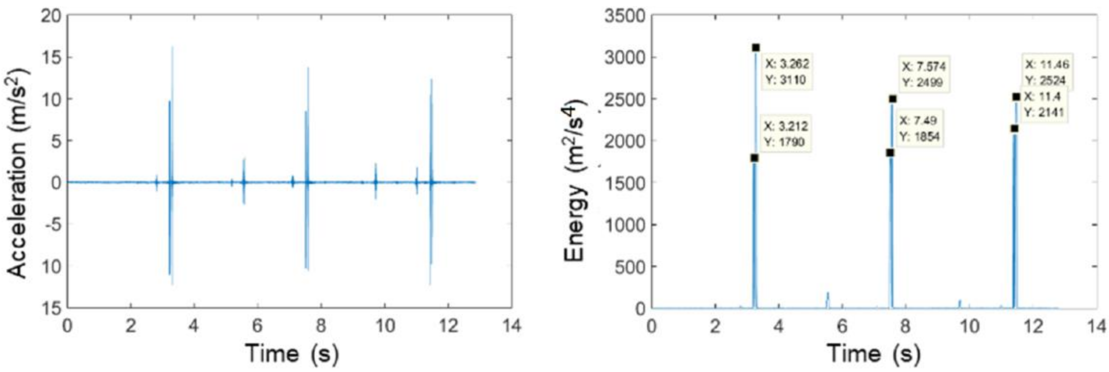


**Figure 19. Short-time energy analysis**

Once the vibration periods were extracted, the TFs were calculated through FFT. Figure 20 plots two examples TFs that correspond to the two transmission directions (at Corner 1). Note that the three curves in each figure denote the results of three repeated measurements at the debonding corner region. It is observed that the three curves match well at the frequency range of

100~500 Hz while significant differences and several abnormal values occur at lower frequencies and higher frequencies. Therefore, we select 100 Hz and 500 Hz as the lower and upper limits, respectively.

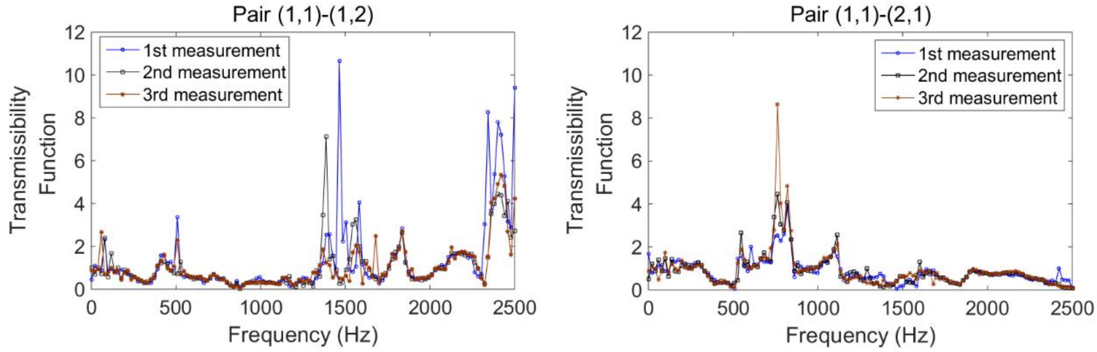


**Figure 20. TFs of three repeated measurements**

*4.4 Results and discussion*

Figure 21 presents the magnitudes of the average TFs that calculated before and after introducing the support-loss. The frequency range is narrowed down to 100~500 Hz. Note that the curves in Figure 21(b) denote the transmissibility functions in the debonding region (Corner 2) while the data in Figure 21(a) is collected in the intact region (Corner 1). It is clearly observed that debonding significantly affects the TFs in the debonding region but slightly affects that in the intact region. The largest difference between the two curves occurs in the frequency range of 100~300 Hz in the debonding region.

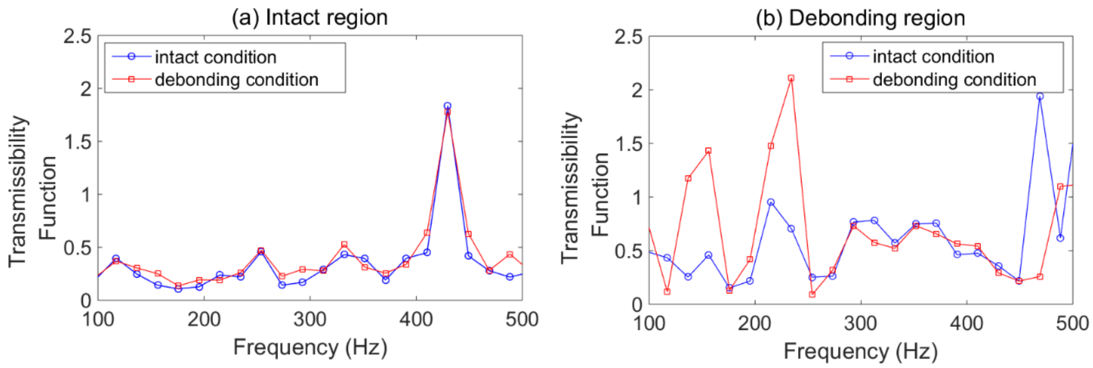


**Figure 21. Comparison of TFs under the intact and debonding regions (at Corner 2)**

The curves in Figure 22 represent the TFs in the edge debonding region (beside Corner 3). It is found observable differences between the two curves in both directions, and the difference in direction 1 (perpendicular) is larger than that in direction 2 (parallel), which demonstrates the results in the FEA.

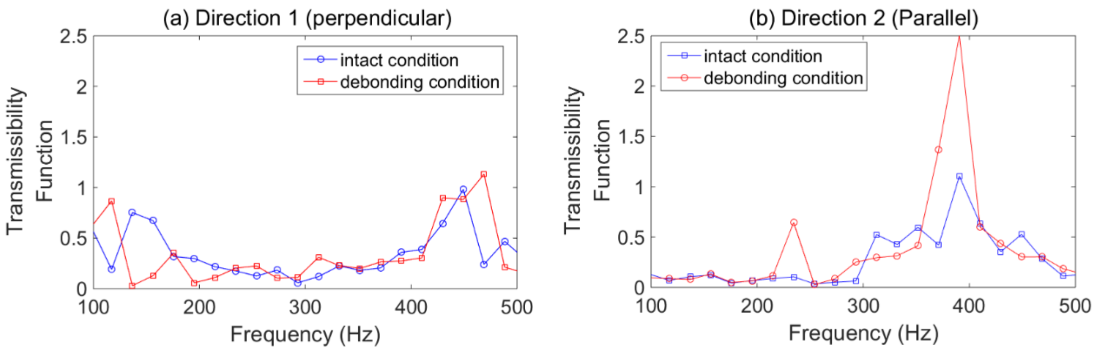


**Figure 22. TFs in the perpendicular direction and parallel direction (debonding edge region)**

The TDI matrices of the two directions are calculated, as plotted in Figure 23. The largest TDI occurs at the node (7,1), which corresponds to the corner debonding region. The TDIs at the two corners are also larger than other TDIs, indicating that the debonding at corners can be easily identified and localized. As expected, the shape of the edge debonding is consistent with the TDI distribution of the $TDI_1$ matrix but does not coincide with that of the $TDI_2$ matrix. However, several TDIs (pair (7,4)-(7,5) in $TDI_1$, pair (5,5)-(6,5) in $TDI_2$) are not as small as expected due to the test error, which may cause misidentification of debonding. Therefore, the TF-based method has the ability to identify and localize debonding at corners but still has certain limitations in detecting and localizing the debonding along the edge.

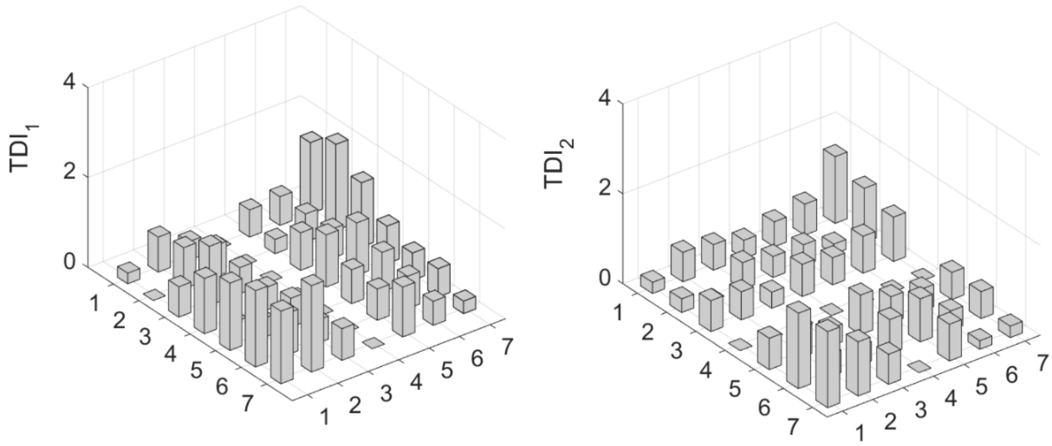


**Figure 23 TDI matrices in debonding condition**

## 5. Conclusion and Discussion

This paper investigated the application of the transmissibility function in detection and localization of debonding under the concrete pavement. The TF-based method was studied and demonstrated in theoretical analysis, finite element analysis, and laboratory tests. In the theoretical analysis, the TF in concrete pavement plate was firstly deduced and discussed. The results indicated that the debonding would significantly affect the TF at higher frequencies. The TF also depends on the debonding position and measurement pair. A local debonding would only affect the TFs measured across the debonding position but have few effects on the transmissibility functions at other positions. Then, a testing procedure and the measurement pair determination for concrete pavement plate TF testing were proposed and analyzed in the finite element analysis and field tests. The results demonstrate the conclusion in theoretical analysis, and it is recommended to apply the TF-based method at a lower noise level (SNR>20 dB) and to use a denser measurement node array. Using two transmissibility damage indicator (TDI) matrices, the distribution of the debonding can be effectively detected and localized. The two matrices perform better for detecting the debonding at the corner region and the edge region but can hardly identify the debonding at the center region of the pavement plate. Transmissibility function analysis was proved to be an effective way for debonding detection and localization in this study, but currently, it still has shortages in real-life applications. Future studies will mainly focus on other structural damage detection in the pavement, such as joint deterioration and microcracks.

## Acknowledgement

This work is funded by National Natural Science Foundations of China (52008309 and 51978520). The authors would also like to thank the referees and editor for very helpful comments.

## Reference

[1] M.I. Darter, K.T. Hall, C.-M. Kuo, Support under Portland cement concrete pavements, 1995.

[2] K. Galal, L. Whiteley-Lagace, FWD / HWD Void Detection Beneath Concrete Pavements or Overlaid Concrete Pavements, SWIFT 2010.Calgary, AB., 2010.

[3] J.A. Crovetti, Deflection-Based Analysis Techniques for Jointed Concrete Pavement Systems, Transportation Research Record. 1809 (2002) 3–11.

[4] E. Song, The Cement Concrete Pavement Detection Based on HHT Experimental Modal Analysis, Chang'an University, Xi'an, China, 2014.

[5] H. Zhao, D. Wu, M. Zeng, Y. Tian, J. Ling, Assessment of concrete pavement support conditions using distributed optical vibration sensing fiber and a neural network, Construction and Building Materials. 216 (2019) 214–226. doi:10.1016/j.conbuildmat.2019.04.195.

[6] T.J. Johnson, D.E. Adams, Transmissibility as a Differential Indicator of Structural Damage, Journal of Vibration and Acoustics. 124 (2002) 634. doi:10.1115/1.1500744.

[7] N.M.M. Maia, R.A.B. Almeida, A.P.V. Urgueira, R.P.C. Sampaio, Damage detection and quantification using transmissibility, Mechanical Systems and Signal Processing. 25 (2011) 2475–2483. doi:10.1016/j.ymssp.2011.04.002.

[8] W. Yan, M. Zhao, Q. Sun, W. Ren, Transmissibility-based system identification for structural health Monitoring : Fundamentals , approaches , and applications, Mechanical Systems and Signal Processing. 117 (2019) 453–482. doi:10.1016/j.ymssp.2018.06.053.

[9] H.P. Zhu, L. Mao, S. Weng, A sensitivity-based structural damage identification method with unknown input excitation using transmissibility concept, Journal of Sound and Vibration. 333 (2014) 7135–7150. doi:10.1016/j.jsv.2014.08.022.

[10] S. Chesné, A. Deraemaeker, Damage localization using transmissibility functions: A critical review, Mechanical Systems and Signal Processing. 38 (2013) 569–584. doi:10.1016/j.ymssp.2013.01.020.

[11] G. Silves, F.B. Veronat, M. Innocenti, M. Napolitano, Fault Detection Using Neural Networks, in: Proceedings of the International Conference on Vibration Engineering, Beijing, 1994: pp. 3796–3799.

[12] L. Cheng, A. Cigada, An analytical perspective about structural damage identification based on transmissibility function, Structural Health Monitoring. (2019). doi:10.1177/1475921719838079.

[13] S. El-Ouafi Bahlous, H. Smaoui, S. El-Borgi, Experimental validation of an ambient vibration-based multiple damage identification method using statistical modal filtering, Journal of Sound and Vibration. 325 (2009) 49–68. doi:10.1016/j.jsv.2009.03.001.

[14] D. Zhu, X. Yi, Y. Wang, New methodology for the application of vibration-based damage detection techniques, Structural Control and Health Monitoring. 23 (2016) 487–502. doi:10.1002/stc.

[15] X. Yi, D. Zhu, Y. Wang, J. Guo, K. Lee, Embedded transmissibility function analysis for damage detection in a mobile sensor network, 7647 (2010) 1–9. doi:10.1117/12.847256.

[16] L. Feng, X. Yi, D. Zhu, X. Xie, Y. Wang, Damage detection of metro tunnel structure through

transmissibility function and cross correlation analysis using local excitation and measurement, Mechanical Systems and Signal Processing. 60 (2015) 59–74. doi:10.1016/j.ymssp.2015.02.007.

[17] J. LI, H. HAO, Damage detection of shear connectors in bridge structures with transmissibility in frequency domain, International Journal of Structural Stability and Dynamics. 14 (2014) 1–33. doi:10.1142/S0219455413500612.

[18] H. ZHANG, M.J. SCHULZ, F. FERGUSON, Structural Health Monitoring Using Transmittance Functions, Mechanical Systems and Signal Processing. 13 (1999) 765–787.

[19] E.M. Godfrin, A method to compute the inverse of an n-block tridiagonal quasi-Hermitian matrix, Journal of Physics: Condensed Matter. 3 (1991) 7843–7848. doi:10.1088/0953-8984/3/40/005.

[20] S. Chun, K. Kim, J. Greene, B. Choubane, Evaluation of interlayer bonding condition on structural response characteristics of asphalt pavement using finite element analysis and full-scale field tests, Construction and Building Materials. 96 (2015) 307–318. doi:10.1016/j.conbuildmat.2015.08.031.